



Article

FIB-SEM Investigation of Laser-Induced Periodic Surface Structures and Conical Surface Microstructures on D16T (AA2024-T4) Alloy

Igor A. Salimon ^{1,*}, Sakellaris Mailis ¹ , Alexey I. Salimon ^{2,*}, Evgenij Skupnevskiy ³, Svetlana A. Lipovskikh ², Iaroslava Shakhova ⁴, Artem V. Novikov ^{2,5}, Timur F. Yagafarov ¹ and Alexander M. Korsunsky ^{2,6} 

¹ Center for Photonics and Quantum Materials, Skolkovo Institute of Science and Technology, Moscow 121205, Russia; S.Mailis@skoltech.ru (S.M.); timur.yagafarov@skolkovotech.ru (T.F.Y.)

² Center for Energy Science and Technology, Skolkovo Institute of Science and Technology, Moscow 121205, Russia; s.lipovskikh@skoltech.ru (S.A.L.); artyom.novikov@skoltech.ru (A.V.N.); a.korsunsky@skoltech.ru (A.M.K.)

³ Lasers & Apparatus Ltd., Zelenograd 124482, Russia; eskypnevskiy@gmail.com

⁴ Advanced Imaging Core Facility, Skolkovo Institute of Science and Technology, Moscow 121205, Russia; y.shakhova@skoltech.ru

⁵ Institute of Problems of Chemical Physics of Russian Academy of Sciences, Chernogolovka 141432, Russia

⁶ MBLEM laboratory, Department of Engineering Science, University of Oxford, Parks Road, Oxford OX1 3PJ, UK

* Correspondence: igor.salimon@skoltech.ru (I.A.S.); a.salimon@skoltech.ru (A.I.S.); Tel.: +7-495-280-14-81 (ext. 3524) (I.A.S.)

Received: 6 December 2019; Accepted: 14 January 2020; Published: 17 January 2020



Abstract: The use of aluminum alloy AA2024-T4 (Russian designation D16T) in applications requiring a high strength-to-weight ratio and fatigue resistance such as aircraft fuselage often demands the control and modification of surface properties. A promising route to surface conditioning of Al alloys is laser treatment. In the present work, the formation of ripples and conical microstructures under scanning with femtosecond (fs) laser pulses was investigated. Laser treatment was performed using 250 fs pulses of a 1033 nm Yb:YAG laser. The fluence of the pulses varied from 5 to 33 J/cm². The scanning was repeated from 1 to 5 times for different areas of the sample. Treated areas were evaluated using focused ion beam (FIB)- scanning electron microscopy (SEM) imaging and sectioning, energy-dispersive X-ray (EDX) spectroscopy, atomic force microscopy (AFM), and confocal laser profilometry. The period of laser-induced periodic surface structures (LIPSS) and the average spacing of conical microstructures were deduced from SEM images by FFT. Unevenness of the treated areas was observed that is likely to have been caused by ablation debris. The structural and elemental changes of the material inside the conical microstructures was revealed by FIB-SEM and EDX. The underlying formation mechanisms of observed structures are discussed in this paper.

Keywords: aluminum alloy 2024; LIPSS; femtosecond laser; conical microstructures

1. Introduction

Laser treatment with femtosecond pulses (fs) has emerged as a topic of intensive investigation due to the recent advances in femtosecond pulse laser availability. Femtosecond lasers are an effective tool for the precision processing of metals [1], having multiple advantages over the more conventional nanosecond pulse lasers. Unlike the latter, which create an extended heat-affected zone, femtosecond pulse lasers can provide a very rapid transition from the solid state to vapor or plasma omitting

melting and the presence of a liquid phase, with only negligible amounts of heat conducted into the surrounding material [2].

Femtosecond laser treatment was also shown to lead to an increase in nanohardness of aluminum and its alloys both under vacuum and in an ambient environment. Processing in the ambient environment oxidation leads to the formation of oxide phases. The concentration of oxygen may reach 16% [3]. Elemental changes in AA2024 with picosecond laser ablation were observed by EDS by Ahuir-Torres et al. [4].

Another feature of femtosecond laser pulse processing is the possible formation of various self-organized structures. The structures emerging at the micro- and nanoscale modify the properties of surfaces, allowing multiple promising applications. They include the creation of superhydrophobic surfaces on stainless steel [5], polymers [6], and silicon [7], drag reduction [8], the creation of self-cleaning surfaces [9], the enhancement of heat transfer [10], chemical sensing [11], and the enhancement of light absorption in gold [12], tungsten, and titanium alloys [13], sulphur-doped silicon [14], and aluminum foil [15]. Possible biological applications include the creation of templates for cellular growth [16] and the enhancement of the stability of dental prosthetics [17].

The formation of self-assembled structures such as laser-induced periodic surface structures (LIPSS) and conical microstructures by exposure to ultrashort pulses has been described for metals [18]. The present work focuses on D16T alloy, the Russian equivalent of AA2024-T4 alloy.

This type of artificially aged Al-Cu alloy is used in aviation because of its attractive mechanical properties (e.g., strength-to-weight ratio) and resistance to mechanical damage.

Near-subwavelength periodic ripples (LIPSS) are commonly referred to as surface self-assembled structures. LIPSS are formed upon the interaction of linearly polarized laser irradiation and solid matter. The incident irradiation is scattered on the random roughness features of the surface, and its interaction with surface-scattered electromagnetic waves and, in some cases, with surface plasmon polaritons leads to inhomogeneous energy absorption. This inhomogeneous energy deposition exhibits strong peaks in the Fourier space and therefore results in the creation of periodic and quasiperiodic structures. Radiation is first absorbed by the electronic system, and then energy is transferred to the lattice [19].

Various phenomena of thermal, chemical, or hydrodynamical nature occur, leading to the spatially modulated removal and redeposition of material. In the case of pulsed incident radiation, the ripples require multiple pulses to fully form, and the pattern of ultimate structure depends on the number of pulses. Thus, the importance of feedback phenomena should be noted. Several aspects of LIPSS formation remain controversial, as discussed in the general literature [20].

LIPSS formation on aluminum was reported in the literature for high [3] and low [21] fluences, including specifically for aluminum alloy AA2024 [22].

The formation of conical microstructures in metals at higher fluences is attributed to the contribution of two mechanisms, namely, preferential ablation and the redeposition of nanoparticles stimulated by ablation. Initially, impurities or defects lead to the formation of small (several microns in size) precursor cones at locations where the material is ablated to a lesser extent. Then, precursor cones grow due to the preferential ablation in the surrounding areas. This preferential ablation is caused by two factors. First, the sloped cone edges (forming an angle with the incident beam) have a larger area for the same irradiation fluence, and therefore ablate less. Second, some of the radiation is reflected from the sloped cone edges to the surrounding areas [18]. This explains the growth of the precursor cones into larger (tens of microns) conical microstructures. The microstructures can even grow above the level of the initial surface due to the redeposition of nanoparticles ablated from furrows between the cones. In the case of the scanning ablation regime, multiple layers of nanoparticles redeposit when the laser beam is moved away, and then are re-melted when the beam returns [18]. Such structures grow both in height and in width, until two cones meet. Then the cones become linked and grow only upwards, while the furrows between them grow deeper downwards [23].

A detailed coverage of conical microstructure growth on aluminum and other metals at 800 nm 130 fs laser pulses is provided by Nayak [24]. More specifically, bump-like microstructures along with maze-like microstructures were observed on AA2024 [25], and the effects of laser fluence and the number of passes on the roughness and reflectivity of ablated areas were examined [26].

One can conclude that the complex character of matter-radiation interaction over a wide range of fluences causes versatile surface topological and microchemical modification for commonly used engineering alloys and offers a promising dedicated procedure for advanced surface enhancement. This highlights the importance of rigorous characterization of surface structures using modern techniques such as focused ion beam (FIB) milling and lamella cutting.

The present work is devoted to the focused investigation of D16T alloy, the Russian equivalent of AA2024-T4 alloy. Using non-destructive atomic force microscopy (AFM) and confocal laser profilometry, high resolution SEM, and FIB milling, we systematically investigated the formed LIPSS and conical microstructures reaching 50 μm in size and covered by nanoparticles, which were created as a result of laser treatment using 250 fs pulses of a 1033 nm Yb:YAG laser. We discuss how laser scan patterns can lead to non-uniform profiles and surface structure variations. Internal non-uniformity of the micrometer-sized cones is first investigated at the nanometer scale using fine FIB-SEM observations.

2. Materials and Methods

The flat surface of a mechanically polished cylinder (diameter 20 mm, height 5 mm) of D16T alloy (Table 1) was treated with laser pulses with fluences varying over the range of 5 to 33 J/cm² (Figure 1a and Table 2). Roman numerals correspond to the fluence of the pulses, from I corresponding to 5 J/cm² to VII corresponding to 33 J/cm².

Table 1. D16T elementary composition.

D16T (AA2024-T4)	Weight %
Al	Balance
Cu	4.239 \pm 0.073
Mg	1.754 \pm 0.037
Mn	0.532 \pm 0.0044
Fe	0.346 \pm 0.011
Si	0.223 \pm 0.0057
Zn	0.152 \pm 0.00071
Ti	0.047 \pm 0.001
Cr	0.016 \pm 0.001

An MLP1-2106 (Lasers & Apparatus Ltd., Zelenograd, Russia) device in a customized commercial setup was used. Scanning of each individual area was achieved by redirecting the beam with a scan head (HurryScan 14, SCANLAB, Puchheim, Germany), whereas switching between different areas was done by moving the stage. The incident laser beam was vertical and linearly polarized along the *y*-axis direction (Figure 1b). The laser source used was Yb:YAG (TETA-10, Avesta, Troitsk, Russia) and had a wavelength of 1033 \pm 3 nm. The initial beam (diameter 12 mm) was focused by an F-theta lens with a 70 mm focus distance. Elongated (1.5 \times 0.5 mm²) rectangular areas were scanned with the laser beam longitudinally in the same *x*-axis direction for all laser beam tracks (Figure 1). The focused beam radius was calculated to be 35 μm . Beam overlap along the scanning lines was calculated to be 34%, whereas the overlap between adjacent scanning lines was 71%.

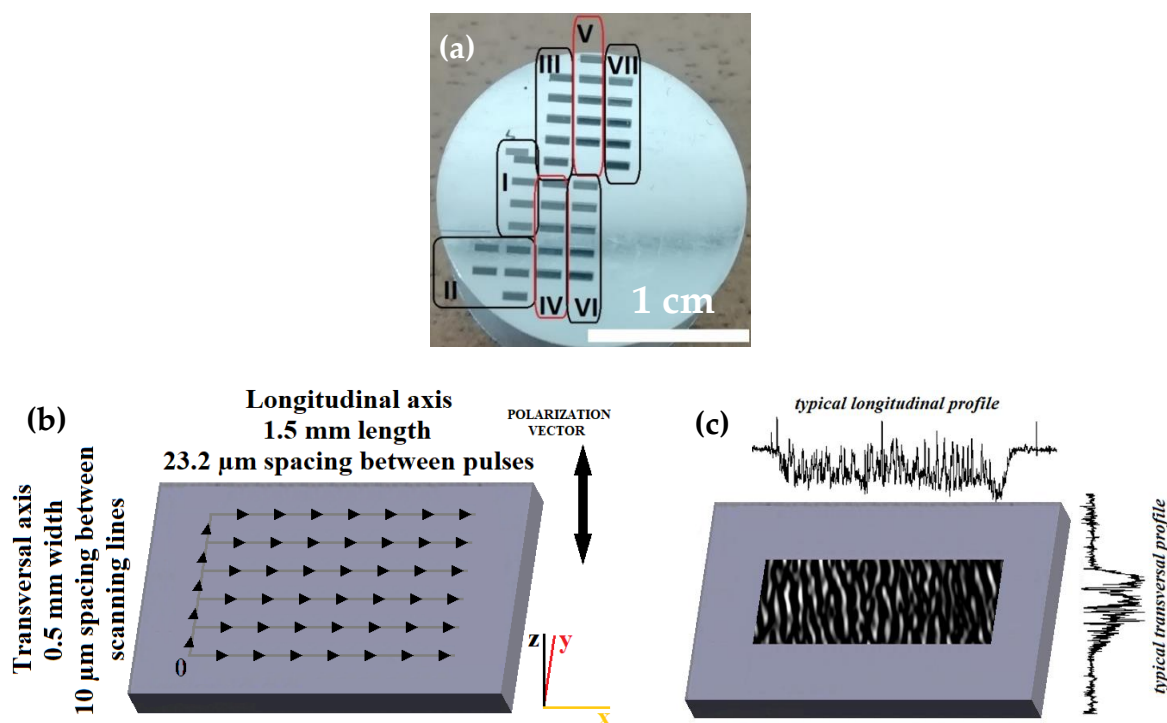


Figure 1. Layout and principal geometry characteristics of laser treatment: (a) photograph of cylindrical D16T sample, with series of treated areas marked; (b) laser scan schematic diagram, with axes defined and scanning (long arrows) and scan progression (short arrows) directions; (c) typical treated area schematic, with laser-induced periodic surface structure LIPSS direction indicated and typical profiles shown.

Table 2. Laser beam spot parameters for different treatment series.

Treatment Series	Pulse Energy, μJ	Energy Fluence, J/cm^2
I	60	5
II	110	9
III	160	13
IV	210	17
V	260	21
VI	310	25
VII	400	33

The pulses had a repetition rate of 25 kHz, which for a 580 mm/s scanning speed gives a $23.2 \mu\text{m}$ distance between separate pulses. The 50 longitudinal scanning lines were separated by a $10 \mu\text{m}$ distance, which is less than the separating distance in the direction of the raster scan. For each value of energy, the scan repetition (SR) number varied from 1 to 5. A PVE300 Photovoltaic Device Characterization System (Bentham Instruments, Reading, UK) was used to estimate the reflectivity in the visible range (300–900 nm). The confocal laser profilometer CCS Optima+ (STIL SAS, Aix-en-Provence, France) with a CL2MG140 optical pen having a z-sensitivity of 40 nm was used for profilometry. Tescan VEGA 3 LMU (Brno, Czech Republic) and Thermo Scientific Quattro ESEM (ThermoFischer, Waltham, MA, USA) devices were used to perform SEM imaging in high vacuum mode. A Thermo Scientific Helios G4 PFIB-SEM UXe DualBeam (ThermoFischer, Waltham, MA, USA) was used for ion milling and lamella preparation. EDX was performed using the Octave Elite Super module (EDAX Inc., Mahwah, NJ, USA). An atomic force microscope SMENA (NT-MDT, Zelenograd, Russia) was used for AFM profilometry. The LIPSS period and average distance between separate cones

in the conical surface microstructures were estimated using ImageJ (1.52a, NIH, Bethesda, MD, USA) (<https://imagej.nih.gov/ij/index.html>) to process SEM and AFM images by means of FFT peak analysis.

3. Results

3.1. Profilometry

Transversal and longitudinal profiles of the ablated areas were investigated by confocal profilometry (Figure 2).

The transversal and longitudinal profiles were clearly different, as the longitudinal profile has its mean line mostly parallel to the sample surface. A dip is observable at the side where the scanning lines start, which is due to the beam not being shut when it switches between scanning lines (Figure 1b). The transversal profile, however, is non-uniform, deeper, and rougher on one side than on the other and therefore its mean line has a noticeable slope. The shallower side corresponds to the side where the laser beam starts the first scanning track. Possible reasons for this effect are discussed later.

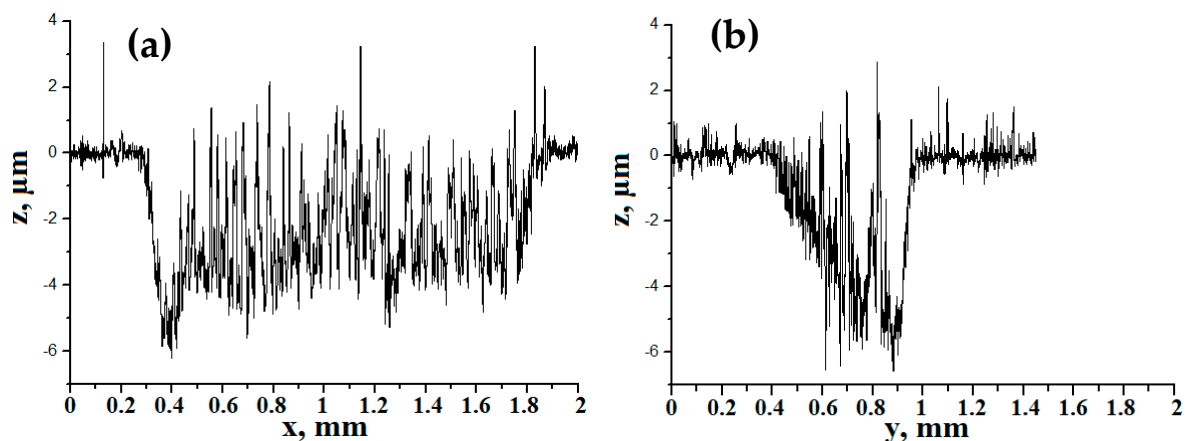


Figure 2. Typical ablation profiles for 21 J/cm². The area with three scan repetitions (SR) was chosen for representation: (a) longitudinal profile of treated area bottom; (b) transversal profile of treated area bottom.

A color-coded chart characterizing the profiles of the treated areas is provided (Figure 3a). The full profiles are presented as Supplementary Materials (Figure S1). The number of scan repetitions varies from 1 to 5 from left to right, the fluence varies from 13 J/cm² to 33 J/cm² from top to bottom. The profiles corresponding to a lower fluence (less than 13 J/cm²) could not be reliably registered because of the low signal-to-noise ratio. AFM and SEM were applied to study these areas.

Three different trends can be deduced from the diagram. First, for 13 J/cm², the profile mean lines are parallel to the surface and they have relatively low roughness until spiky peaks appear at higher numbers of pulse repetitions; that range is marked in green. An example profile is provided (Figure 3b). The depth of the profiles increases monotonously with the number of pulses (Figure 4a).

Second, at a higher energy treatment, the spiky peaks are not yet identifiable on the profiles after smaller numbers of pulse repetitions, but the profile mean lines are noticeably sloped; those profiles are marked in yellow. An example profile is provided (Figure 3c). The mean slope angle of the profile increases with both energy and the number of pulse repetitions (Figure 4b). The slope angle is small but always positive. The 21 J/cm² one-repetition treated area is excluded, since it was too close to the edge and was curved due to polishing.

Finally, at high values of energy and numbers of pulse repetitions, the profiles reveal abrupt peaks and dips, and their height increases with energy and number of pulse repetitions. Those profiles are marked in red. An example profile is provided (Figure 3d). In general, such transversal profiles show

uneven roughness—the peak-dip pattern is deeper and rougher at the side of the treated area where the laser beam was scanning later.

R_a and R_z roughness parameters were calculated for the profiles (Tables 3 and 4, respectively).

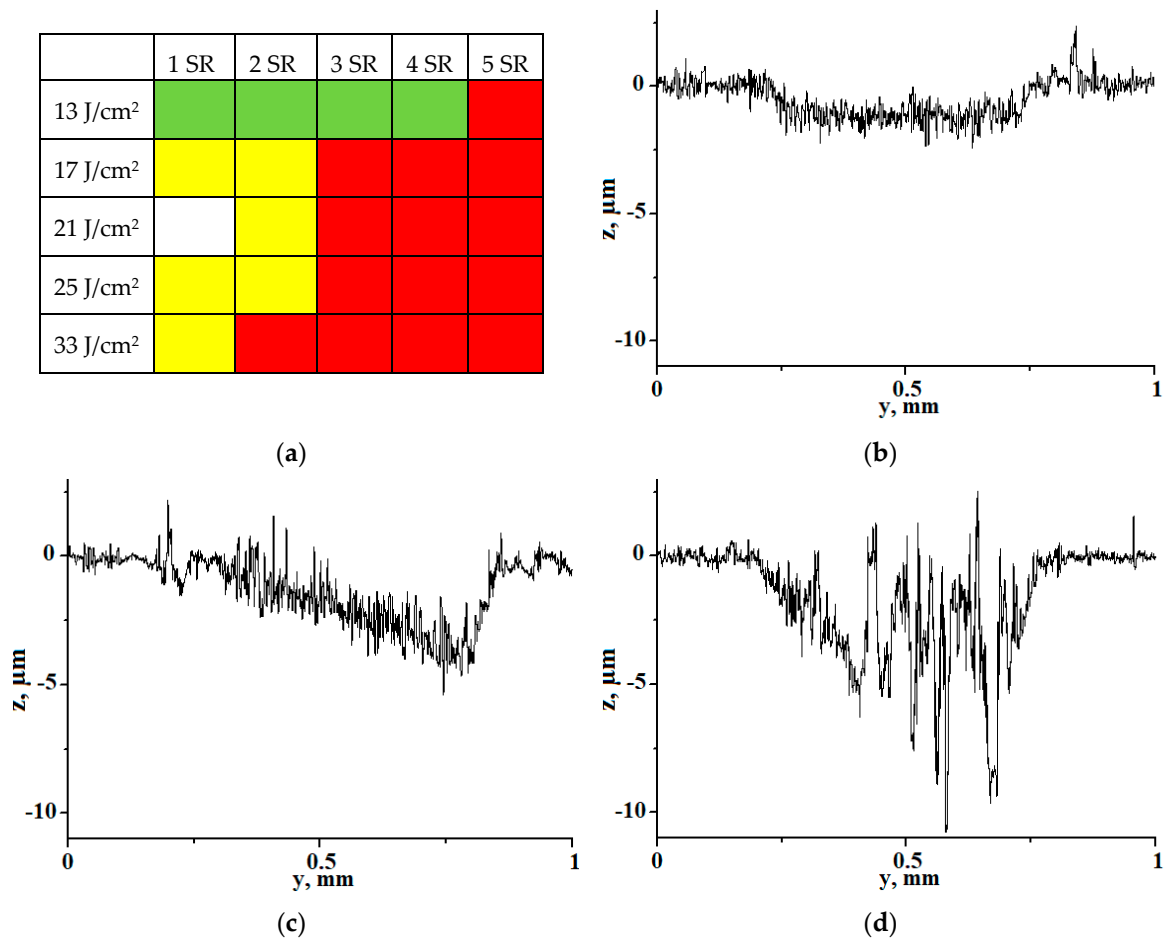


Figure 3. Profiles of laser-treated areas: (a) color-coded chart; (b) example profile for “green” profiles which are parallel to the initial surface; (c) example profile for “yellow” profiles with an observable slope; (d) example profile for “red” profiles with high roughness. SR: scan repetition.

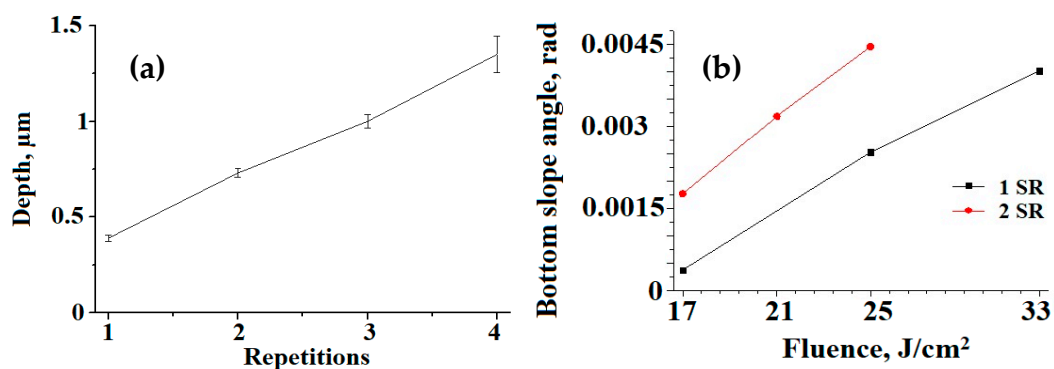


Figure 4. Profile parameters: (a) depth of laser-treated areas at 160 μJ ; (b) average slope angle of treated area bottom.

Table 3. R_a roughness parameter for laser-treated areas, nm.

Fluence, J/cm ²	1 Scan Repetitions	2 Scan Repetitions	3 Scan Repetitions	4 Scan Repetitions	5 Scan Repetitions
13	249	219	242	310	744
17	237	247	412	1146	773
21	300	413	661	793	1423
25	364	395	598	1302	1541
33	381	735	1666	1132	1133

Table 4. R_z roughness parameter for laser-treated areas, μm .

Fluence, J/cm ²	1 Scan Repetitions	2 Scan Repetitions	3 Scan Repetitions	4 Scan Repetitions	5 Scan Repetitions
13	4.5	3.8	3.2	6.7	14.3
17	4.5	2.8	8.0	12.1	9.5
21	2.8	6.8	8.1	13.0	18.8
25	6.4	4.6	8.6	20.6	18.2
33	4.3	7.1	23.0	16.7	18.3

3.2. LIPSS: SEM Imaging and Analysis

The collage of SEM images characterizing the appearance of treated areas is given in Figure 5 as a function of laser beam energy and number of scan repetitions. Treated areas are generally darker than the surrounding alloy surface. SEM reveals two types of surface motifs formed by femtosecond laser ablation—the relatively even surface is populated with periodic ripples (LIPSS) resolvable at higher magnifications and rough and bright grainy clusters constructed by conical microstructures. Both motifs may be simultaneously present in the treated area; however, generally the conical microstructure is characteristic of a higher beam energy and a higher number of scan repetitions, that is, larger doses of treatment energy applied. The portion of conical microstructure in the treated area is always greater at higher values of y , that is, for the last scan tracks, which strongly correlates with the data for treated area profiles. Separate single cones appear relatively randomly over the surface of treated areas at low fluence and the smaller number of scan repetitions, but they are more frequent at larger y values and may even occur outside the treated area. We believe that the main mechanism triggering the formation of conical microstructures is the redeposition of ablated material; however, the intensity of ablation is stimulated by laser treatment at neighboring tracks, and therefore an avalanche (or chain reaction) effect takes place when the redeposition of material at previous tracks enhances the ablation at the current track and the redeposition at the next track.

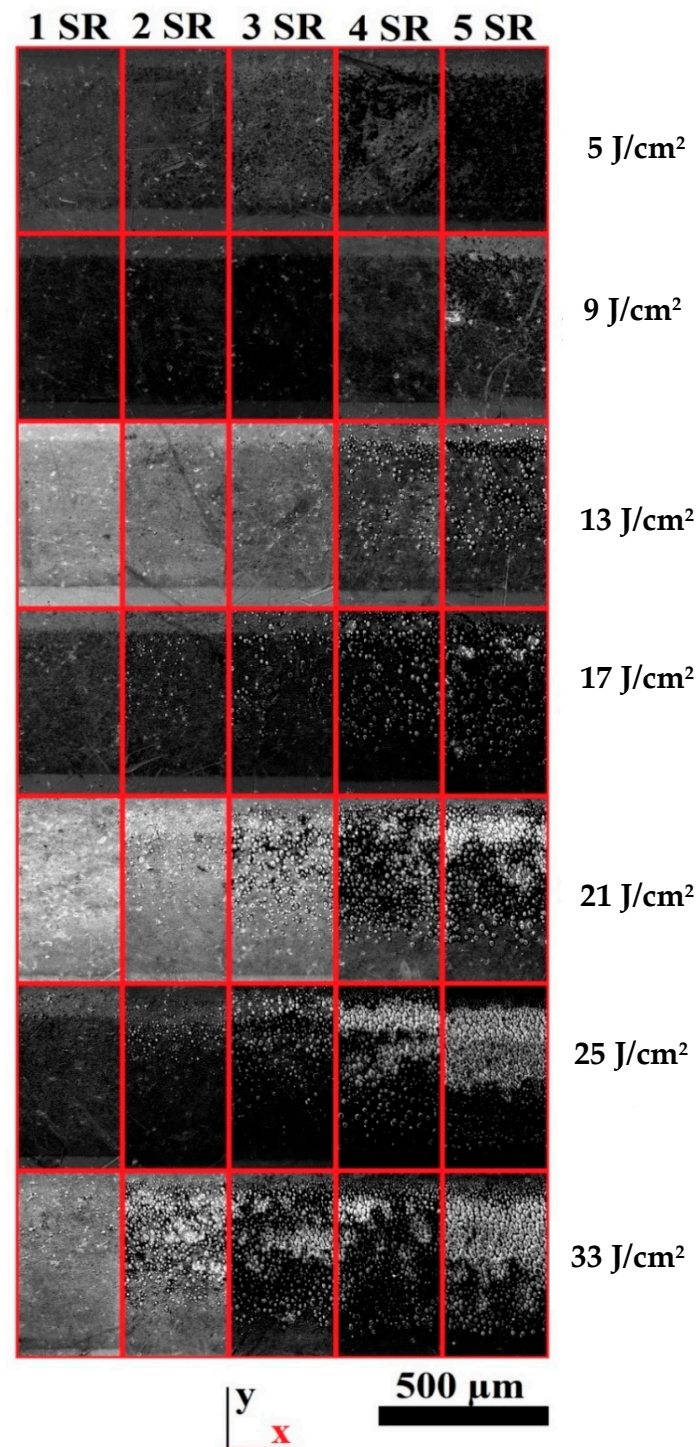


Figure 5. Appearance of laser-treated areas.

On the other hand, at low fluence the most representative structures are the LIPSS (Figure 6a,d). The SEM images in secondary electrons had a satisfactory contrast of the ripples, allowing the determination of their period using FFT image processing. The area treated with 9 J/cm^2 fluence with the scanning repeated 5 times is depicted as an example (Figure 6a,b). The LIPSS having obvious periodicity exhibit some irregularity (Figure 6a), which is also demonstrated by the broad peak at the FFT spectrum (Figure 6c,d). The LIPSS period for this area is equal to $0.78 \pm 0.13 \text{ } \mu\text{m}$. This value within

the range of standard deviation was found to be invariant for all studied treated areas showing almost no dependence on fluence and scan repetitions.

A granular structure of the ripples, however, is visible at high magnification (Figure 6b). Perhaps, these granules resulted from the redeposition process, and some of them may play a role as cone precursors during an ongoing laser treatment.

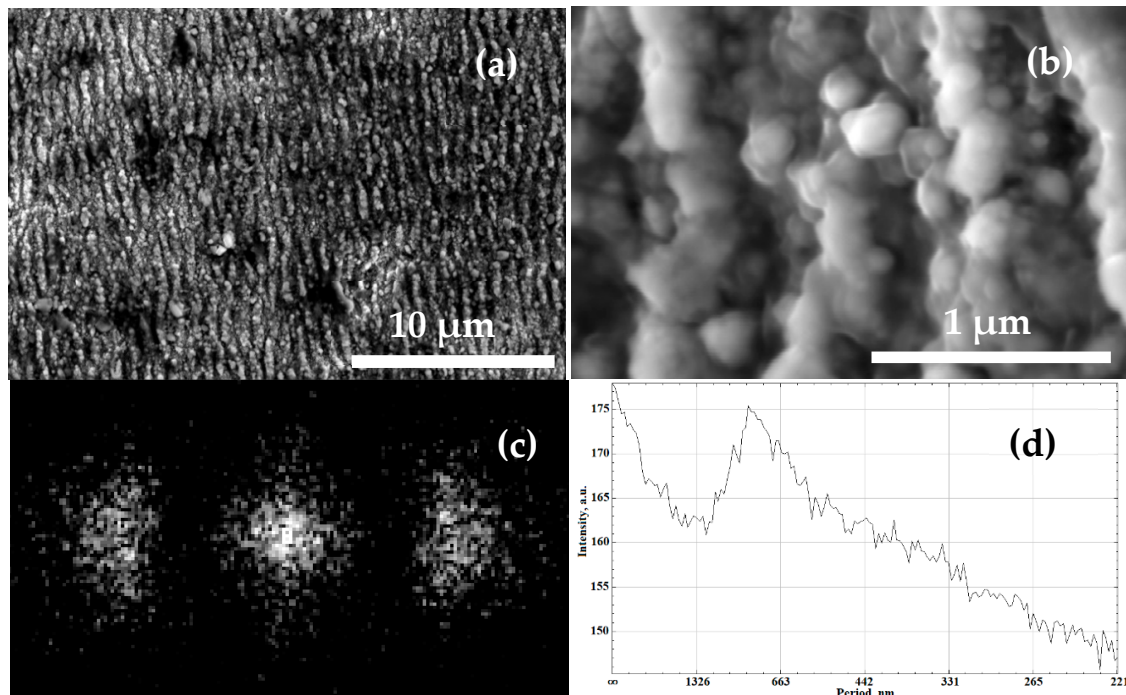


Figure 6. SEM images for 9 J/cm^2 with five scan repetitions. (a) Wide shot SEM demonstrating periodic yet loosely regular LIPSS; (b) SEM close-up on LIPSS, revealing a granular structure (observed with 52° sample tilt); (c) FFT of initial SEM image with contrast enhanced; (d) FFT spectrum with the peak clearly visible.

3.3. LIPSS: AFM Profilometry and Analysis

Laser confocal profilometry cannot resolve the LIPSS formed at the lowest energy regime. Therefore, the characteristics of periodic ripples formed at a fluence of 5 J/cm^2 were studied by AFM (Figure 7).

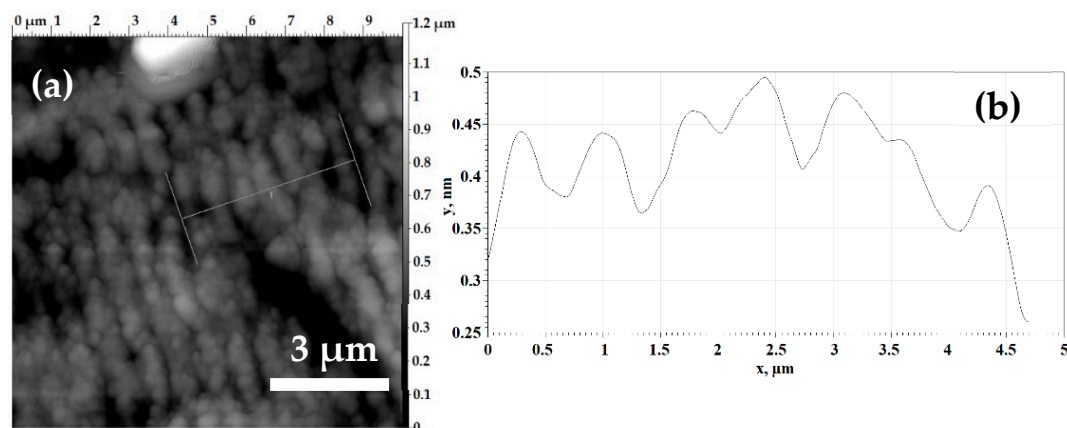


Figure 7. AFM profiling of LIPSS for 5 J/cm^2 with three scan repetitions: (a) topography image of a $10 \times 10 \mu\text{m}^2$ area; (b) linear profile along a direction perpendicular to the LIPSS (dashed line).

The calculated LIPSS periods and peak heights are given in Table 5.

Table 5. Period and height of LIPSS per fluence.

Fluence, J/cm ²	Number of Repeats	LIPSS Period, μm	LIPSS Height, nm
5	3	0.8 ± 0.09	83.0 ± 14.5
5	5	0.8 ± 0.07	116.8 ± 24.9

3.4. Conical Microstructure Imaging and Analysis

The increase of energy and number of pulses leads to the emergence and growth of conical microstructure clusters and the simultaneous depletion of the LIPSS area.

For the laser treatment at 13 J/cm² fluence, the conical microstructures become noticeable even after a single scan (Figure 6). With the rise of pulse energies and numbers of repetitions, the conical microstructures cover an increased portion of the treated area. Moreover, SEM imaging of the conical microstructures indicates that the increase of fluence and number of pulses tends to enhance the aspect factor of a single cone. For example, for the twice-repeated 21 J/cm² fluence laser treatment, the conical microstructures are represented by 2.5–3 μm high and less than 10 μm wide cones, whereas for the 33 J/cm² fluence and five repetitions, cones reach a height of 30 μm and a width of 20–25 μm (Figure 8a). A pattern of lines is observable on the slopes of some conical structures (Figure 8b). These lines are most likely LIPSS.

The focused ion beam (FIB) cutting of a cone grown after the treatment at 33 J/cm² fluence with five scan repetitions reveals that the content of the tip is different from that of the bulk of the alloy (Figure 8e).

A comparison between SEM images acquired before and after cleaning in an ultrasonic bath in acetone and isopropanol is shown in Figure 8c,d. After cleaning, the removal of the loose layer of nanoparticles can be observed on the slopes.

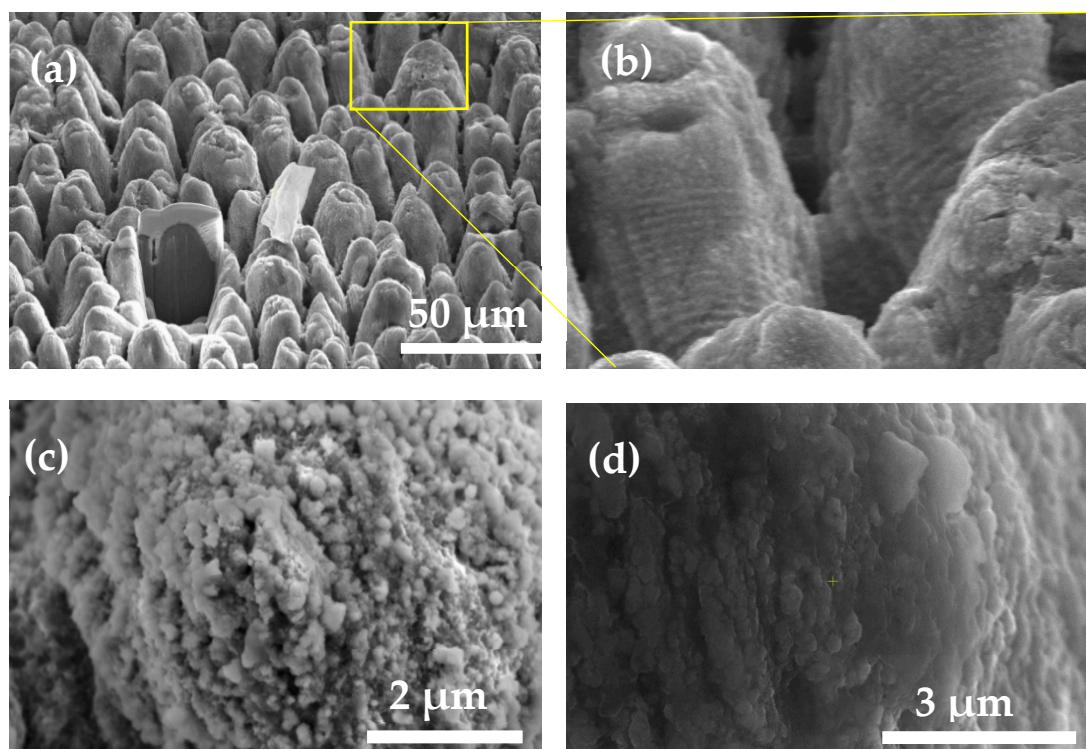


Figure 8. *Cont.*

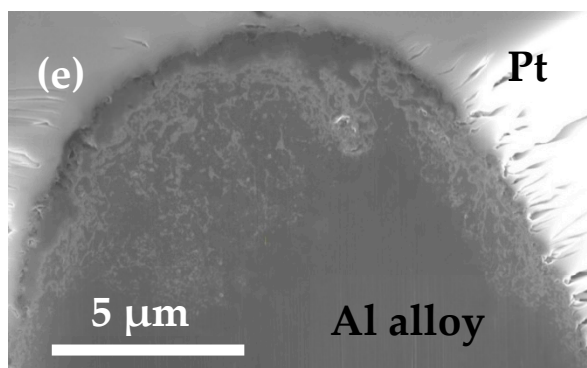


Figure 8. SEM images of conical microstructures for 33 J/cm² with five scan repetitions: (a) conical microstructures (observed with 52° sample tilt), with an impurity particle and the site of FIB milling; (b) close-up of the conical structures' slopes with the contrast enhanced, ripples are observable (observed with 52° sample tilt); (c) tip of a conical microstructure before cleaning in acetone; (d) slope of a conical microstructure after cleaning in acetone; (e) internal content of a conical structure sectioned in half by FIB (observed with 52° sample tilt), a protective layer of platinum is deposited on top.

By analyzing the position of the small and wide peak in the FFT spectrum, it was possible to estimate the average distance between the cone tops in the conical structures (Figure 9b). The cones are surrounded by deep furrows, which gives a recognizable pattern of dark lines (Figure 9a). The peak in the FFT spectrum does not represent true periodicity, but identifies the most frequent distance between two furrows (Table 6).

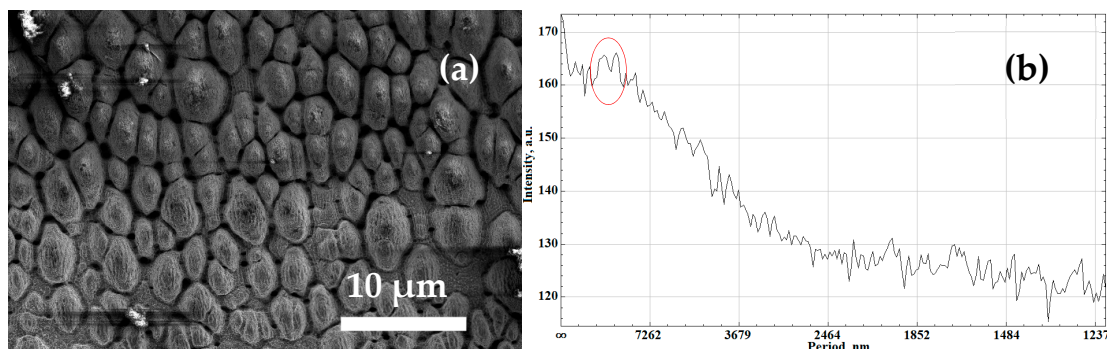


Figure 9. Image analysis for conical microstructures for 21 J/cm² with five scan repetitions: (a) SEM image with conical microstructures; (b) fourier transform graph with a peak corresponding to the average conical structure size marked in red.

Table 6. Average distance between cone tops per fluence.

Fluence, J/cm ²	Number of Repeats	Conical Microstructures' Average Distance, μm
21	5	11.55 ± 3.91
25	5	18.46 ± 2.21
33	5	15.43 ± 3.86

The internal structure of a cone formed by laser ablation treatment at 33 J/cm² with five scan repetitions was investigated by FIB cross-sectional cutting. A protective Pt layer was applied to avoid curtaining defects. The cut (Figure 10a) was analyzed by EDX (Figure 10b–d), then a thin lamella was cut out for higher resolution SEM (Figure 10e) and EDX (Figure 10f–h) imaging. An interesting area with a brighter SEM signal, deep oxidation, and a reduced Al EDX signal is observable in the cross-section and is marked in red (Figure 10a–c). Further features worth consideration can be seen in the thin lamella imaged using SEM and EDX. The feature marked in yellow (Figure 10e–h) reveals

an area of darker SEM signal (Figure 10e), an enclave with higher Al concentration (Figure 10f), and a pore. The pore gives a bright signal in the Al EDX image due to multiple electron scattering (Figure 10f). Both the aluminum enclave and the pore show a “shadow” of reduced Cu and O concentration (Figure 10g,h). The anomaly outlined in white is most likely a pore (Figure 10e–h). The black-circled anomaly (Figure 10e–h) does not exhibit noticeable SEM contrast, but EDX reveals a higher concentration of Cu (Figure 10h) and a decrease in Al concentration (Figure 10g).

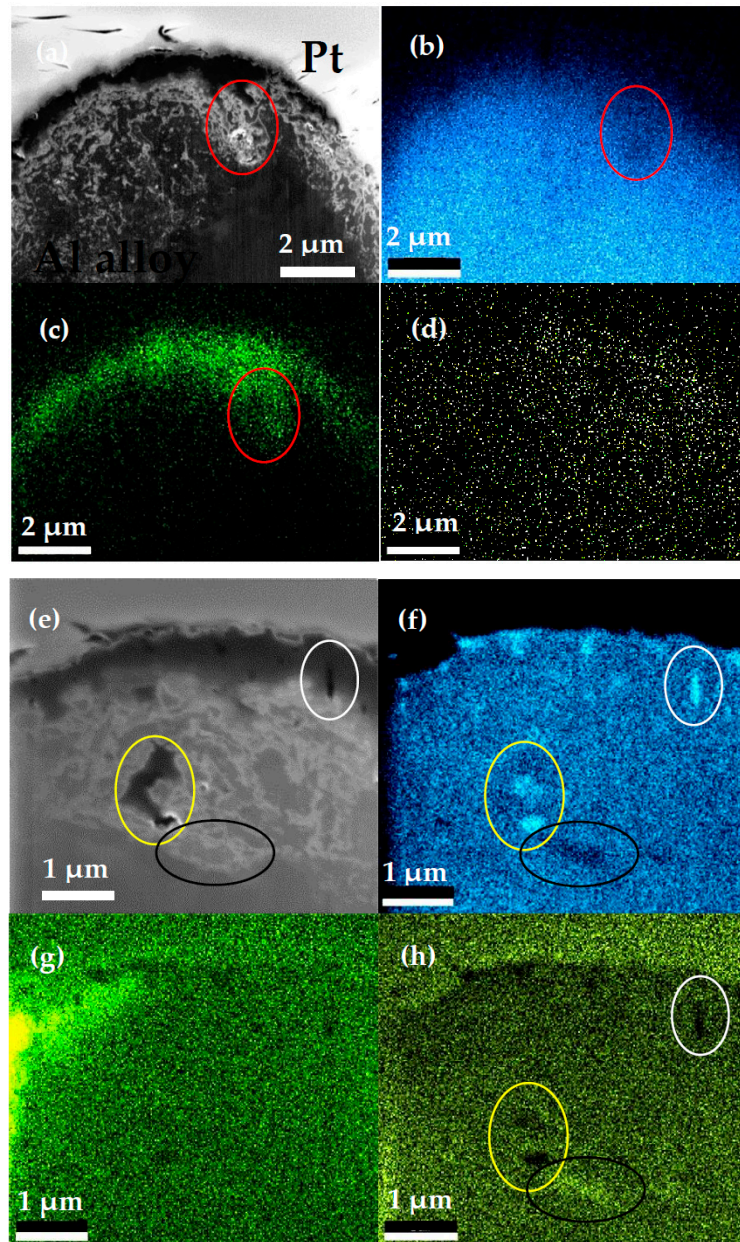


Figure 10. FIB sectioning of a cone formed by laser ablation treatment at 33 J/cm^2 with five scan repetitions: (a) SEM image of FIB-cut conical structure; (b) EDX showing Al concentration inside the FIB-cut conical structure; (c) EDX showing O concentration inside the FIB-cut conical structure; (d) EDX showing Cu concentration inside the FIB-cut conical structure; (e) SEM image of lamella cut from the conical structure; (f) EDX showing Al concentration inside the lamella cut from the conical structure; (g) EDX showing O concentration inside the lamella cut from the conical structure; (h) EDX showing Cu concentration inside the lamella cut from the conical structure. Contrast is enhanced for all images.

4. Discussion

We believe that the slope of the mean bottom line and the uneven roughness of the treated areas are caused by the influence of redeposited ablated material. Ablated material from the areas exposed to the earlier laser pulses partially redeposits to the areas that are exposed later. This leads to decreased light reflectivity of the latter areas and, as a result, their higher absorption and more intensive further ablation. Moreover, this increases the probability of forming conical microstructures, since the redeposited nanoparticles make the ablation less uniform causing a positive feedback for cone growth in a self-stimulating process. Thus, conical structures starting to grow earlier at the edge of the treated area will have a higher aspect ratio, leading to non-uniform roughness. This effect may be undesirable for engineering applications.

The influence of redeposited ablated material on the formation of conical microstructures was described by Zuhlke et al. [18] in detail. Ablated nanoparticles redeposit when the beam is away, and later, when the scanning beam reaches them again, a portion of the nanoparticles melts. This forms a structure with alternating layers of melted and non-melted particles. The similarity between this work and our work is confirmed when we clearly observe that the conical structures appear to be covered with the layer of sharp nanoparticles, while ultrasonic bath cleaning with acetone removes any loose layer of nanoparticles.

AA2024 that is ablated to the point of conical structure growth has been demonstrated to be a broadband absorber [26]. We could easily observe this in our work. The low reflectivity can be observed with the naked eye, as the treated areas look black (Figure 1a). The decrease in reflectivity was approximately evaluated by an integrating sphere measurement. The sphere PVE300 illuminated a spot of 1 mm diameter that was obviously bigger than the width of the treated area; therefore, the signal was collected from both the treated area and the surrounding untreated surface. The untreated alloy's surface showed a reflectivity of $79 \pm 5\%$ in the visible light (300–900 nm) wavelength range, whereas the spot that was positioned in the center of the laser-treated area illuminating both the laser-treated area and the untreated surrounding alloy had an integral reflectivity of $42 \pm 2\%$ within the same wavelength range. Applying the linear rule of mixture to the contributions of treated and untreated areas, it was possible to estimate the reflectivity of the treated area as $21 \pm 2\%$.

LIPSS with a 703 nm period were observed on AA2024 in a very recent work for a scan with an 800 fs pulse 1030 nm laser [22]. Similarly, LIPSS on aluminum are mentioned in the work of Umm-i-Kalsoom et al. [3]. Those LIPSS were observed at much higher fluences for a treatment conducted using a 30 fs pulse duration and an incident laser wavelength of 800 nm.

Bashir et al. observed LIPSS on Al for low energy fluences, 25 fs pulses, and an 800 nm incident wavelength. The authors concluded that the LIPSS observed were due to the excitation of surface plasmon polaritons and that the period of the structures depended sensitively on the material selected and the laser fluence [21].

In our work, the LIPSS that we observed were irregular and their period Λ seemed to show no dependence on fluence in the range we observed, equaling approximately to $0.73 \cdot \lambda$ (λ —laser wavelength of 1033 nm). Accordingly, these LIPSS should be attributed to the category of low spatial frequency LIPSS (LSFLs), having a period higher than $0.5 \cdot \lambda$. Existing theories explain the formation of LSFLs by the interference of the incident laser pulses and the surface-scattered electromagnetic waves [20].

A detailed coverage of conical microstructure growth on aluminum and other metals at 800 nm 130 fs laser pulses is presented by Nayak and Gupta [24]. A focused ion beam (FIB) cutting of a conical structure grown on titanium is provided, with no internal structural change was observed. Conical structures grown on aluminum exhibited less regularity than the ones created on stainless steel and titanium.

Bump-like microstructures along with maze-like microstructures were observed on AA2024 [25]. Models were proposed to fine-tune the laser irradiation parameters for the better reproduction of a desired type of microstructure. The differences in the surface structures observed on

different metals were explained by differences in the strength of electron-phonon coupling and the thermal conductivities.

Another work providing significant insight into the properties of microstructures grown on AA2024 via femtosecond ablation examines the effect of laser fluence and number of passes on the roughness and reflectivity of ablated areas [26].

Finally, it is worth mentioning the work revealing the contents of an onion-like aggregated nanoparticle sphere on AA2024 via focused ion beam milling [27].

In our case, we supposed that the observed conical structures and deep valleys surrounding them were mostly caused by preferential ablation of lower areas, as described in [18]. However, while this does define the high aspect ratio of the conical structures for the most part, this is not the only mechanism of structure growth, because profilometry reveals the presence of microstructures higher than the initial surface level. This is most likely caused by the redeposition of ablated material on the cone tops, where less ablation occurs compared to other areas.

While detailed research of conical microstructure growth on AA2024 has already been conducted, to the best of our knowledge, no attempts have been made to study the internal contents of the conical microstructures using FIB-SEM and conducting an EDX study of a lamella cut from the tip of a conical structure. A research paper has conducted an EDX study of the surface of ablated AA2024 [4]. However, there are significant differences between that work and ours. Exposures were static (no scanning was conducted). In that work, it was shown that more significant elemental change and oxidation were observed at the rim of laser impact and not in the center [4].

Section 3.4. of this paper provides insight into the structure of the tip of a conical microstructure, grown above the initial surface by redeposition. EDX data reveals the oxidization of treated areas as deep as 3 μm inside the conical microstructures (Figure 10c). Areas of increased concentration of O and Cu are observed with the respective depletion of Al concentration (Figure 10b,f), and vice versa. The inhomogeneous distribution of O, Cu, and Al inside the tip can be caused by a number of overlapping possible mechanisms. Stain-like patterns visible inside the lamella cannot be easily explained by changes in elemental concentration or a change in density.

The formation of conical microstructures and LIPSS can be speculatively thought of as dissipative structures similar to Rayleigh-Bénard cells which are formed in non-equilibrium conditions of energy and mass transport within the system. Particular shapes, aspects and sizes of the Rayleigh-Bénard cells are the stationary solutions of parametrical differential equations specific for the particular processing conditions. It can be anticipated that other than conical types of structures formed at laser ablation treatment can be created using the technique presented herein [28].

5. Conclusions

Femtosecond pulse laser treatment of metal alloys represents a number of advantages for the gentle and tunable advanced surface enhancement at an industrial scale. The complex multimodal modification of reflectivity, hydrophobicity, nanohardness, and corrosion resistance can be implemented through purposeful surface structuring. LIPSS and surface conical structures having particular topology and size characteristics are formed in certain ranges of parameters, such as laser wavelength, pulse energy, and total fluence. Femtosecond pulse laser treatment of widely applied aged Al-Cu alloys (2024-T4 or Russian equivalent D16T) is of particular practical interest for systematic characterization and research in technological parameter optimization.

We applied both traditional non-destructive AFM, confocal laser profilometry, and high-resolution SEM and modern techniques such as FIB milling and lamella cutting to fill the gaps in the understanding of self-assembled surface structure formation mechanisms. We found that, under laser treatment using 250 fs pulses of a 1033 nm Yb:YAG laser, the unevenness of treated areas occurred at lower fluences (5 J/cm²) in the form of LIPSS developing toward conical structures, which were highly likely formed as a result of redeposited ablation material from earlier stages of ablation affecting later ablation in other areas. In contrast to other reports, LIPSS with periods of 0.73λ were observed parallel to the incident

irradiation direction. No clear dependence of LIPSS characteristics on laser treatment parameters was observed. Overall, the increase of laser fluence or pulse number (SR) gave rise to the formation conical microstructures. The increment of fluence enhanced the area of conical microstructures and overall roughness. The height of cones reached 20–30 μm and the altitude of some cones surpassed the initial surface level, which indicates redeposition mechanisms of growth in addition to preferential ablation. FIB-SEM observations facilitated with EDX revealed that the ablation and redeposition processes were responsible for internal non-uniformity and chemical inhomogeneity at the nanometer scale in the top 3–5 μm of the cone structures. Corrosion tests were considered to assess the effect of copper enrichment on the top of the cones.

Both LIPSS and conical structures caused a significant decrease in reflectivity of the treated areas. We believe that the modification of both chemical and optical surface properties ultimately expands the application diversity for AA2024 after this type of relatively simple, fast, and low-cost surface treatment.

Supplementary Materials: The following are available online at <http://www.mdpi.com/2075-4701/10/1/144/s1>, Figure S1: Profiles of laser-treated areas.

Author Contributions: Conceptualization, I.A.S., A.I.S., and A.M.K.; Data curation, I.A.S. and T.F.Y.; Formal analysis, A.I.S. and A.M.K.; Funding acquisition, A.M.K.; Investigation, I.A.S., S.A.L., A.V.N., and T.F.Y.; Methodology, E.S. and A.V.N.; Resources, E.S.; Software, I.A.S. and E.S.; Supervision, S.M., A.I.S., and A.M.K.; Validation, I.S. and A.V.N.; Visualization, I.A.S., S.A.L., I.S., and A.M.K.; Writing—original draft, I.A.S. and A.I.S.; Writing—review and editing, S.M., A.I.S., and A.M.K. All authors have read and agreed to the published version of the manuscript.

Funding: The authors received no external funding.

Acknowledgments: Authors are grateful to Advanced Imaging Core Facility of Skoltech for valuable assistance in FIB-SEM imaging, to M. Chichkov (Shared Facility Center of NUST MISIS, Moscow, Russia) for valuable insight in profilometry, and P.A. Troshin (Center for Energy Science and Technology, Skolkovo Institute of Science and Technology, Moscow, Russia) for useful discussions about AFM data.

Conflicts of Interest: The authors declare no conflict of interest.

References

1. Banks, P.S.; Stuart, B.C.; Perry, M.D.; Feit, M.D.; Rubenchik, A.M.; Armstrong, J.P.; Nguyen, H.; Roeske, F.; Lee, R.S.; Myers, B.R.; et al. Femtosecond laser machining. *Tech. Dig. Conf. Lasers Electro-Opt.* **1998**, *6*, 510.
2. Momma, C.; Chichkov, B.N.; Nolte, S.; Alvensleben, F.V.; Tunnermann, A.; Welling, H.; Wellegehausen, B. Short-Pulse laser ablation of solid targets. *Opt. Commun.* **1996**, *129*, 134–142. [[CrossRef](#)]
3. Umm-i-Kalsoom; Ali, N.; Bashir, S.; Begum, N.; Rafique, M.S.; Husinsky, W. Morphological, elemental and hardness analysis of femtosecond laser irradiated Al targets. *Opt. Laser Technol.* **2018**, *108*, 107–115. [[CrossRef](#)]
4. Ahuir-Torres, J.I.; Arenas, M.A.; Perrie, W.; de Damborenea, J. Influence of laser parameters in surface texturing of Ti6Al4V and AA2024-T3 alloys. *Opt. Lasers Eng.* **2018**, *103*, 100–109. [[CrossRef](#)]
5. Wu, B.; Zhou, M.; Li, J. Superhydrophobic surfaces fabricated by microstructuring of stainless steel using a femtosecond laser. *Appl. Surf. Sci.* **2009**, *256*, 61–66. [[CrossRef](#)]
6. Nayak, B.K.; Caffrey, P.O.; Speck, C.R.; Gupta, M.C. Superhydrophobic surfaces by replication of micro/nano-Structures fabricated by ultrafast-Laser microtexturing. *Appl. Surf. Sci.* **2013**, *266*, 23–32. [[CrossRef](#)]
7. Baldacchini, T.; Carey, J.E.; Zhou, M.; Mazur, E. Superhydrophobic surfaces prepared by microstructuring of silicon using a femtosecond laser. *Langmuir* **2006**, *22*, 4917–4919. [[CrossRef](#)]
8. Ahmmed, K.M.T.; Kietzig, A.-M. Drag reduction on laser-Patterned hierarchical superhydrophobic surfaces. *Soft Matter* **2016**, *12*, 4912–4922. [[CrossRef](#)]
9. Zorba, V.; Stratakis, E.; Barberoglou, M.; Spanakis, E.; Tzanetakis, P.; Anastasiadis, S.H.; Fotakis, C. Biomimetic artificial surfaces quantitatively reproduce the water repellency of a lotus leaf. *Adv. Mater.* **2008**, *20*, 4049–4054. [[CrossRef](#)]

10. Kruse, C.M.; Anderson, T.; Wilson, C.; Zuhlke, C.; Alexander, D.; Gogos, G.; Ndao, S. Enhanced pool-Boiling heat transfer and critical heat flux on femtosecond laser processed stainless steel surfaces. *Int. J. Heat Mass Transf.* **2015**, *82*, 109–116. [[CrossRef](#)]
11. Li, G.; Lu, Y.; Wu, P.; Zhang, Z.; Li, J.; Zhu, W.; Hu, Y.; Wu, D.; Chu, J. Fish scale inspired design of underwater superoleophobic microcone arrays by sucrose solution assisted femtosecond laser irradiation for multifunctional liquid manipulation. *J. Mater. Chem. A* **2015**, *3*, 18675–18683. [[CrossRef](#)]
12. Vorobyev, A.Y.; Guo, C. Enhanced absorptance of gold following multipulse femtosecond laser ablation. *Phys. Rev. B* **2005**, *72*, 195422. [[CrossRef](#)]
13. Vorobyev, A.Y.; Guo, C. Black metals through femtosecond laser pulses. In *AIP Conference Proceedings*; AIP: College Park, MD, USA, 2012; Volume 1464, p. 397.
14. Crouch, C.H.; Carey, J.E.; Shen, M. Infrared absorption by sulfur-Doped silicon formed by femto second laser irradiation. *Appl. Phys. A* **2004**, *79*, 1635–1641. [[CrossRef](#)]
15. Hwang, T.Y.; Vorobyev, A.Y.; Guo, C. Enhanced efficiency of solar-Driven thermoelectric generator with femtosecond lasertextured metals. *Opt. Express* **2011**, *19*, A824. [[CrossRef](#)] [[PubMed](#)]
16. Straub, M.; Uchugonova, A.; Koch, M.; König, K. Silicon cell culture templates with nanotopography: Periodic nanostructures and random nanoporous topologies generated by high-Repetition rate sub-15 fs pulsed nearinfrared laser light. *Proc. SPIE-Int. Soc. Opt. Eng.* **2012**. [[CrossRef](#)]
17. Orazi, L.; Maksym, P.; Deineka, V.; Husak, E.; Korniienko, V.; Mishchenko, O.; Reggiani, B. Osteoblast Cell Response to LIPSS-Modified Ti-Implants. *Key Eng. Mater.* **2019**, *813*, 322–327. [[CrossRef](#)]
18. Zuhlke, C.A.; Troy, P.A.; Dennis, R.A. Fundamentals of layered nanoparticle covered pyramidal structures formed on nickel during femtosecond laser surface interactions. *Appl. Surf. Sci.* **2013**, *283*, 648–653. [[CrossRef](#)]
19. Sipe, J.E.; Young, J.F.; Preston, J.S.; Van Driel, H.M. Laser-Induced periodic surface structures. I. Theory. *Phys. Rev. B* **1983**, *27*, 1141–1154. [[CrossRef](#)]
20. Bonse, J.; Hohm, S.; Kirner, S.V.; Rosenfeld, A.; Kruger, J. Laser-Induced Periodic Surface Structures-A Scientific Evergreen. *IEEE J. Sel. Top. Quantum Electron.* **2017**, *23*, 9000615. [[CrossRef](#)]
21. Bashir, S.; Rafique, M.S.; Husinsky, W. Femtosecond laser-Induced subwavelength ripples on Al, Si, CaF₂ and CR-39. *Nucl. Instrum. Methods B* **2012**, *275*, 1–6. [[CrossRef](#)]
22. Zhanga, H.Z.; Wanga, H.Y.; Liub, F.F.; Wangc, L. Investigation on femtosecond laser ablative processing of SiCp/AA2024 composites. *J. Manuf. Proc.* **2020**, *49*, 227–233. [[CrossRef](#)]
23. Li, Y.; Cui, Z.; Wang, W.; Lin, C.; Tsai, H.-L. Formation of linked nanostructure-textured mound-shaped microstructures on stainless steel surface via femtosecond laser ablation. *Appl. Surf. Sci.* **2013**, *324*, 775–783. [[CrossRef](#)]
24. Nayak, B.K.; Gupta, M.C. Self-Organized micro/nano structures in metal surfaces by ultrafast laser irradiation. *Opt. Lasers Eng.* **2010**, *48*, 940–949. [[CrossRef](#)]
25. Tanvir Ahmmed, K.M.; Jee Yang Ling, E.; Servio, P.; Kietzig, A.-M. Introducing a new optimization tool for femtosecond laser-Induced surface texturing on titanium, stainless steel, aluminum and copper. *Opt. Lasers Eng.* **2015**, *66*, 258–268. [[CrossRef](#)]
26. Singh, N.; Alexander, D.R.; Schiffrin, J.; Doerr, D. Femtosecond laser production of metal surfaces having unique surface structures that are broadband absorbers. *J. Laser Appl.* **2006**, *18*, 242–244. [[CrossRef](#)]
27. Tsubaki, T.A.; Kottenb, M.A.; Lucis, M.J.; Zuhlke, C.; Ianno, N.; Shield, J.E.; Alexander, D.R. Formation of aggregated nanoparticle spheres through femtosecond laser surface processing. *Appl. Surf. Sci.* **2017**, *419*, 778–787. [[CrossRef](#)] [[PubMed](#)]
28. Khmelevskaya, V.S.; Malynkin, V.G. Anomalous states in metallic alloys induced by irradiation. *Phase Trans.* **1997**, *60*, 59–65. [[CrossRef](#)]

